Bioprinting 28 (2022) e00242

Contents lists available at ScienceDirect

Bioprinting

journal homepage: www.sciencedirect.com/journal/bioprinting

Non-planar embedded 3D printing for complex hydrogel manufacturing

Benjamin J. Albert [a], Coral Wang [b], Christian Williams [c], Jonathan T. Butcher [a,*]

[a] Meinig School of Biomedical Engineering, Cornell University, Ithaca, NY, 14853, United States
[b] Sibley School of Mechanical and Aerospace Engineering, Cornell University, Ithaca, NY, 14853, United States
[c] Department of Materials Science and Engineering, Northwestern University, Evanston, IL, 60208, United States

ARTICLE INFO

Keywords:
Non-planar bioprinting
Tissue engineering
Alginate
Embedded printing
FRESH

ABSTRACT

Embedded bioprinting as a tissue engineering method has expanded the ability to bioprint complex geometry of native tissue. Print bath support in these methods allows the biomaterial to solidify in place, mitigating the possibly negative effects of low viscosity and gravity. This material stability also permits for non-planar deposition of the biomaterial. Here, we developed a non-planar 3D print slicer for non-planar embedded bioprinting. We quantified the changes in ink deposition properties with respect to non-planar movement to understand printability in the system. Alginate prints in a FRESH support bath were used to quantify the capability of the slicer to create tunable mechanical properties. Mechanical testing reveals that geometric changes to the printed models can tune stiffness, failure stress and strain, and Poisson's ratio. These results demonstrate that using non-planar manufacturing can produce mechanically tunable properties with a homogeneous biomaterial. This may strengthen our ability to precisely match mechanical properties of native tissues to improve tissue engineering outcomes.

1. Introduction

The introduction of 3D printing methods into the field of tissue engineering has expanded the possibilities of tissue manufacturing [1–4]. The increase in 3D bioprintable materials and methods has led to rapid advances in the field [5,6]. However, there are still many hurdles to overcome for many clinical applications of bioprinting [7]. Manufacturing tissues out of cellularly viable materials has been difficult because most biomaterials require an external factor to solidify the material to maintain its manufactured shape [8]. Extrusion printing methods have often been used for bioprinting because of the wide range of materials that can be extruded through this deposition method [9,10]. This printing process requires thermal, chemical, UV crosslinking, or other methods to solidify the extruded material to maintain the desired structure [3,4]. When printing in open air, these materials may collapse or deform before the solidification can take effect [11–13]. In situ methods of crosslinking and printing have expanded the clinical applications of bioprinted tissue; however, these methods require the support of the underlying tissue to maintain shape and must be printed directly into a patient [14,15]. Recent advances in embedded printing have increased the resolution capability of extrusion bioprinting by holding the deposited material in place to allow for more time to solidify [16–18]. These methods rely on a secondary bath of material that the biomaterial is extruded into. The rheological properties of the bath material hold the printed material in place relative to where it was deposited. This method has allowed for creation of complex vessels, heart valves, and additional structures that have been difficult to replicate with open air extrusion bioprinting [17,19]. The support of the bath ensures that the printed material is unaffected by gravity, meaning that the printing direction is only constrained by the capabilities of the printer [20].

Traditional print slicing software for 3-axis printers is limited to printing a complete layer in the X–Y plane and then translation in the Z axis to start the next layer. Geometries that are discontinuous in any particular X–Y slice require travel moves between extrusion sites that may blend and distort the deposited material. A similar effect may be seen when printing with multiple materials in embedded printing methods. Extruder changes require removal of the current nozzle from the bath and insertion of a second nozzle. These travel moves may additionally disrupt the deposited material either through the nozzle itself or material oozing during travel moves.

Planar slicing can recreate many structures with embedded printing; however, the material deposition is limited to a single X–Y plane at any given time. Many tissues are composed of organic curves that may not be

* Corresponding author. Meinig School of Biomedical Engineering, Cornell University, Ithaca, NY, USA.
E-mail address: jtb47@cornell.edu (J.T. Butcher).

https://doi.org/10.1016/j.bprint.2022.e00242
Received 6 June 2022; Received in revised form 25 August 2022; Accepted 12 September 2022
Available online 24 September 2022

conducive to being sliced in this way. Tissues often contain multiple domains of materials and often within a curved structure (e.g. trachea, intervertebral disc, heart valves) [21–23]. In addition, these materials often align to create anisotropic properties that can be replicated through utilizing the print nozzle direction [24,25]. Controlling print curvature to match the natural curvature of a tissue may allow for control over material deposition and mechanical properties.

Recent studies have demonstrated non-planar printing, where the print path direction is not constrained to the X–Y plane, of thermoplastics and hydrogels to create thin, curved materials with a preferred print path direction [15,26]. However, these printed materials still rely on a static pre-determined support for the print to be deposited onto. Embedded printing of biomaterials allows for similar strategies to be implemented for bioprinting applications without the need for separate support structures. In this study, we present a new method of slicing 3D bioprint models for non-planar movement to create a variety of structures applicable to tissue engineering. We describe the process of developing non-planar prints for embedded printing using a novel surface slicing method using a visual programming language. Next, this method is compared with traditional slicing and the advantages that this new method creates. We then explore the capabilities of this method with respect to print mechanics. Overall, this study demonstrates the ability to tune mechanical properties and create complex materials using traditional bioinks with this non-planar printing method.

2. Materials and methods

2.1. Non-planar print slicer

The non-planar slicer was developed in the visual programming language of Dynamo Studio (Autodesk, Inc.). The process is visually described in Fig. S1. To begin, a surface of the desired geometry is imported into the script. Planes are generated in the X-Z and Y-Z axes at increments equal to the desired print path width. These planes are intersected with the surface to generate lines on the surface that represent the major paths. The ends of the major paths are connected by a nearest neighbor algorithm to generate continuous paths within a layer. The result is a single, complete layer of paths that fills the entire footprint of the surface with a continuous print path. The two sets of paths generated by slicing in the perpendicular X-Z and Y-Z planes are offset to create the first two layers of the print. These layers are duplicated in an alternating fashion to create the full, desired thickness of the print. Prints can also be created to contain a single path direction where all layers are composed of parallel paths. Extrusion values in the GCODE are calculated by finding the distance between sequential points on the paths and multiplying the distance by a predetermined scalar that represents the desired amount of extrusion (based on nozzle size, material viscosity, print speed, etc.). The points that comprise the path are converted to strings and combined with the extrusion values to create the lines of a GCODE file. Extruder changes are inserted into code where a material change is desired, and the resulting set of strings is exported to a GCODE file. Prints were sliced with 0.4 mm path width, 0.3 mm layer height, and six layers unless otherwise noted.

2.2. Bioprinter

Printing was done using a modified Ender 3 (Creality) printer. The stock motherboard was swapped to a MKS Gen L v1.0 for dual extruder capabilities. A second Z-axis motor was added to stabilize both ends of the gantry during vertical motion. Two Replistruder V3 [17] extruder systems were modified to attach to the printer gantry.

2.3. Printing with FRESH v2.0

Alginate (Protanal LF10/60, FMC Biopolymer) was prepared by dissolving 4% w/v in deionized water. 1% India ink was added for visualization in certain applications.

Freeform reversible embedding of suspended hydrogels (FRESH) support bath was prepared as previously described [17,27]. Briefly, 20 g of gelatin (Type B, 100 Bloom, Fisher Scientific) was dissolved in 500 mL of distilled water and 500 mL of 100% ethanol at 40 °C. 2.5 g of Pluronic F127 (MW ~12,600, Sigma-Aldrich) and 1.0 g of gum Arabic (Ward's Science) were subsequently dissolved in the solution. The pH was adjusted to 6 and stirred overnight while cooling to room temperature. The solution was aliquoted to 50 mL tubes and centrifuged at 400 rpm for 5 min. Supernatant was poured off and the remaining solution was resuspended in distilled water and centrifuged for 5 min at 1500 rpm.

Supernatant was again poured off and the solution was washed with 0.1% calcium for alginate printing. The solution went through a third centrifugation at 1500 rpm for 5 min and was resuspended in 0.1% calcium chloride. It was then stored at 4 °C until printing.

Before printing, FRESH bath was mixed and placed in a vacuum chamber to come to room temperature. FRESH bath was then centrifuged at 1600 rpm for 5 min, the supernatant was poured off, and the FRESH bath was poured into the print container.

Post-print processing was performed by placing the print container into a 37 °C oven for at least an hour to melt the FRESH bath. Prints were then washed with 2% $CaCl_2$ at least three times to fully crosslink the alginate and remove excess FRESH.

2.4. Multi-material planar and non-planar printing

Two syringes of 4% alginate were prepared: one pure alginate and one with 1% India ink. An "M"-shaped surface was created for non-planar slicing and an equivalent solid was created for slicing using Ultimaker Cura (Ultimaker BV). Prints were created using both slicers with three layers of black, three layers of clear, and three layers of black. Both were printed into a glass-walled container and a video of both prints was recorded. The print bath was then melted and washed away. Samples were then photographed.

2.5. Print angle quantification

Prints were conducted by extruding 4% alginate into FRESH bath with a 25-gauge needle (McMaster-Carr) in a glass-paned vessel. Nine different angle prints were designed such that multiple lines (0°, 22.5°, 45°, 67.5°, 90°, −22.5°, −45°, −67.5°, −80°) could be produced in one print. In a cycle, the extruder translates horizontally, then upwards at the programmed angle, then horizontally, then down at the programmed angle, until the length of the vessel is spanned. Afterwards, the FRESH bath was melted in a 37 °C oven and washed with 2% $CaCl_2$. Images of the prints were taken through a microscope and analyzed in ImageJ.

2.6. Printing and mechanical testing of corrugations

Flat and corrugated prints were 44 mm long and 16 mm wide. Corrugations were printed with six layers (0.3 mm per layer) of 4% alginate with print paths running along the length of the geometry unless otherwise specified.

Samples were mounted onto a custom tensile test device using 3D printed, textured clamps that hold onto the flat ends of the prints. Samples were taken out of solution, mounted, and immediately stretched to 20% strain at a rate of 1.0 mm/s. A 50 g force sensor (LSB200, FUTEK Advanced Sensor Technology, Inc.) measured the response to stretch, and the resulting stress was calculated based on the cross section of the samples. Initial modulus was calculated up to 10% strain for each sample and maximum modulus was found at the maximum slope of the stress-strain curve. Ultimate tensile strength (UTS) was measured by finding the stress at sample failure.

2.7. Features of corrugated structures

Prints of varying amplitude, fillet radius, and size of corrugated features were created. Amplitude was varied by starting with a base model of five periods with 45° corrugations and reducing the amplitude of features by 0.5x, 0.25x, and 0x.

Fillet diameter was varied by taking the same base model and changing the baseline fillet diameter (0.5 mm) to 0 mm, 1 mm, and 2 mm. This effectively changes the sharpness of the print motion at the peaks and valleys of the geometry.

Size and frequency of corrugations was varied by changing the number of periods within the same length of geometry. The angle of corrugation was maintained at 45° and fillet diameter was 0.5 mm. These geometries contain 0 (flat), 2.5, 5, and 10 periods of corrugation within them.

2.8. Print path direction of corrugated structures

A five-period corrugation with 0.5 mm fillets was sliced with the six print layers aligned in varying directions. Layers align parallel or perpendicular to the length (direction of mechanical stretch). Five prints were generated with 0, 2, 3, 4, or 6 layers aligned in the direction of stretch. Alternated layers were aligned perpendicular to the direction of stretch.

2.9. Miura-Ori origami geometry

Miura-Ori [28] surface geometries were created with the same dimensions as the simple corrugations. Geometries contained folds with a depth of 0, 2, 4, and 6 mm. After printing and washing, samples were stretched to 20% strain for ten cycles. Initial modulus was calculated up to 10% strain for each sample and modulus was found at the maximum slope of the stress-strain curve. The Poisson ratio was calculated using the initial width and the width at 20% strain.

2.10. Statistical analysis

Data was analyzed using one way ANOVA followed by Tukey's multiple comparisons test. Values are presented as mean ± standard deviation. Statistical significance is defined as $P \leq 0.05$ (*), $P \leq 0.01$ (**), $P \leq 0.001$ (***), or $P \leq 0.0001$ (****).

3. Results

3.1. Development of non-planar slicer

Our slicer can replicate CAD surface models with continuous print paths that follow non-planar travel (Fig. 1). The slicer can handle continuous and discontinuous surfaces if no point occurs directly above another on the initial surface geometry. The slicer can create paths on either one axis or on two perpendicular axes to create a cross-hatching pattern between alternating layers. 3D surfaces are created by duplicating layers to the desired print thickness.

3.2. Effect of extruder direction on alginate extrusion width

Bright-field microscopy was used to measure extrusion width of alginate extruded in multiple directions. As shown in Fig. 2, measurement of path width with respect to printed angle demonstrates that upward motion leads to no significant difference in path width compared to horizontal movement. Downward movements of 45° and greater display extrusion widths greater than the nozzle diameter. The steeper the downward angle, the greater the diameter and the more variable the measurements.

3.3. Multi-material printing with non-planar and planar slicing

The non-planar method follows the curvature of the model to maintain the fidelity of the final print while the planar sliced model builds up the geometry in slices of the Z-axis (Fig. 3B and C). Travel moves are required between parts of the structure that are at the same height in the Z-axis. Accumulation of material is apparent in the top left of the planar print.

The non-planar print extruders travel along the curvature of the model, depositing material without any travel moves within a layer (Fig. 3D, Video S2). There are only two extruder changes during the print when switching from black to clear and then back to black. There is very little excess material accumulation in the container. There is a very distinct differentiation between the three layers except at the lowest center point of the print.

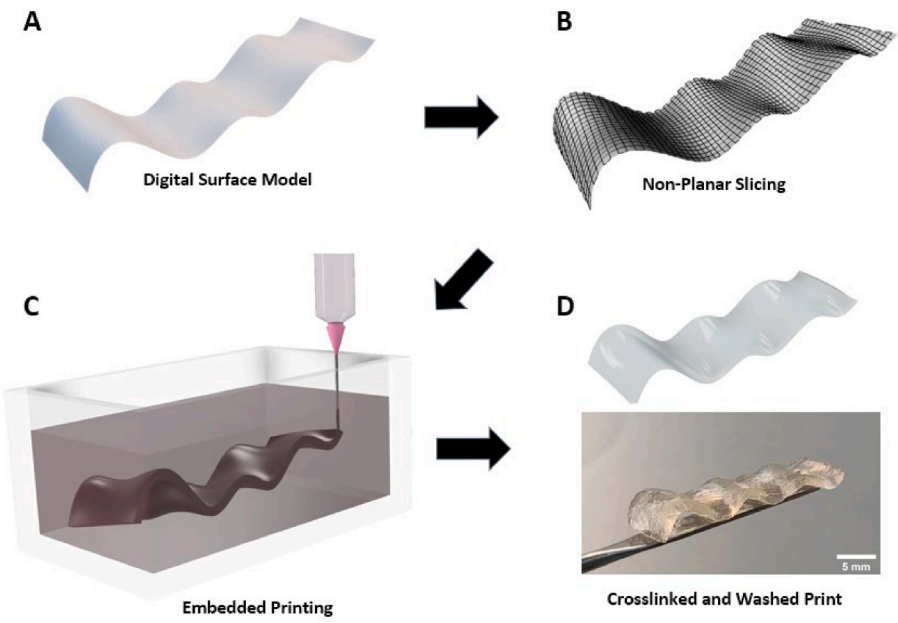

Fig. 1. The process of generating a non-planar print. (A) A digital surface model of the desired geometry that is imported as an STL file. (B) Paths are generated using planes that intersect with the surface model in either the X or the Y direction. Layers are repeated to generate the desired final thickness. (C) The print GCODE is loaded to the bioprinter, and the print is created in an embedded print bath. (D) The print is then washed of the bath and the result is a solid print with the curvature of the initial model.

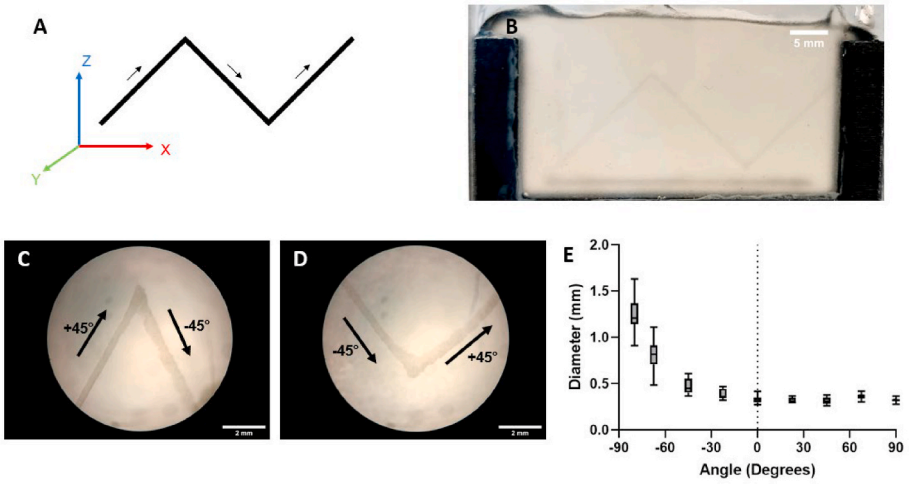

Fig. 2. Print path consistency depends on print angle. (A) Example of print path scheme for measuring +45° and −45° angles. (B) Representative image of 45° print. (C) Representative paths of 45° upward (+45°) printing transitioning to 45° downward (−45°) printing. (D) Representative paths of 45° downward (−45°) printing transitioning to 45° upward (+45°) printing. (E) Print path diameter with respect to print angle.

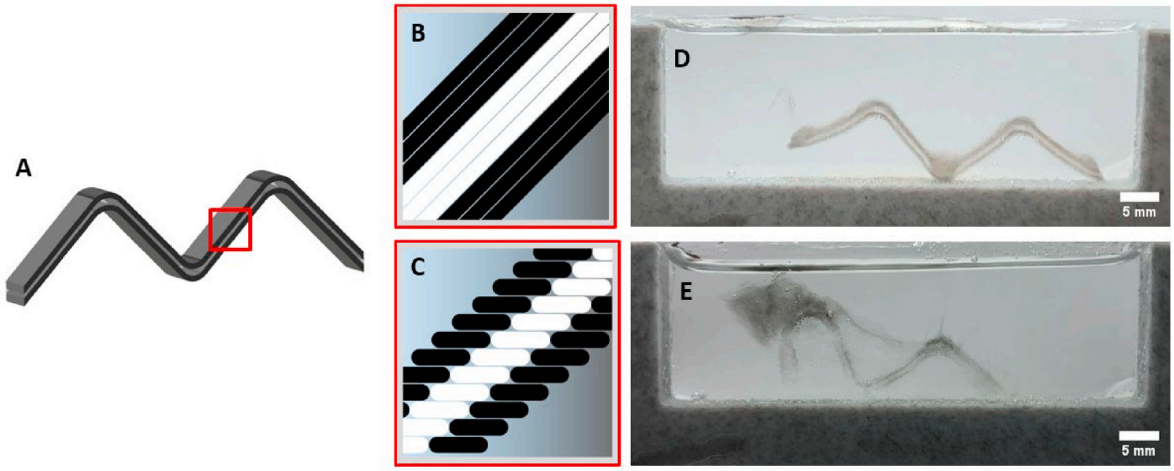

Fig. 3. Dual material planar and non-planar printing of a layered curve. (A) Model of the alternating layers with the "M"-shaped curve. (B) Representation of the non-planar print paths. (C) Representation of the planar print paths. (D) Final print with non-planar slicing. (E) Final print with planar slicing.

3.4. Mechanics of corrugated alginate prints

Amplitude of the corrugation was altered from flat prints to 45° angle corrugations with 0.5 mm fillet diameter (Fig. 4A and B). The prints are described by their amplitude relative to that of the 45° angle print; that group has a value of one and amplitudes decrease incrementally down to zero (flat prints). After printing, the prints were stretched to failure to quantify their mechanical properties (Fig. 4C). Increasing the amplitude of the prints lowers the initial modulus of the prints (Fig. 4D and E). Corrugations also trend towards upward J-shaped curves. The maximum modulus of the flat samples is greater than that of the corrugated samples, with the trend decreasing with greater amplitude (Fig. 4F). A similar trend is seen with the ultimate tensile stress (Fig. 4G). Plotting strain at failure (Fig. 4H) shows that mid-range corrugated amplitudes reduce the failure strain but it returns to that of flat samples at high amplitudes.

Fillet diameter was similarly altered in the base corrugated geometry to understand how the folds further contribute to the mechanical response to stretch (Fig. 5A). The fillet diameter ranged from 0 mm (90° intersection) to 2 mm (Fig. 5B). With stretch to failure, we found that increasing the fillet diameter creates a higher initial modulus and reduced strain stiffening (Fig. 5C and D). The maximum modulus and ultimate tensile stress show no significant trends with respect to the fillet diameter (Fig. 5E and F). Strain at failure (Fig. 5G) shows the 0.5 mm fillet trends towards increasing the strain at failure while increasing the fillet diameter significantly lowers it further.

Lastly, we created several variations on the base corrugation by altering the number of periods contained within the same sample length. The intersections were kept at 45° for all samples, leading to high corrugation amplitude in low periodicity samples and vice versa (Fig. 6). Lower periodicity created greater strain stiffening and significantly lower initial modulus. However, lower periodicity also reduces the maximum modulus and ultimate tensile strength. Strain at failure of 5 period and 2.5 period does not significantly change compared to the flat sample.

3.5. Effect of path direction on response to stretch

To study the effect of path direction on the mechanics of alginate prints, the same base corrugation was printed as previously described. However, path direction was modified depending on the sample. Direction ranged from all six paths perpendicular to the axis of stretch to

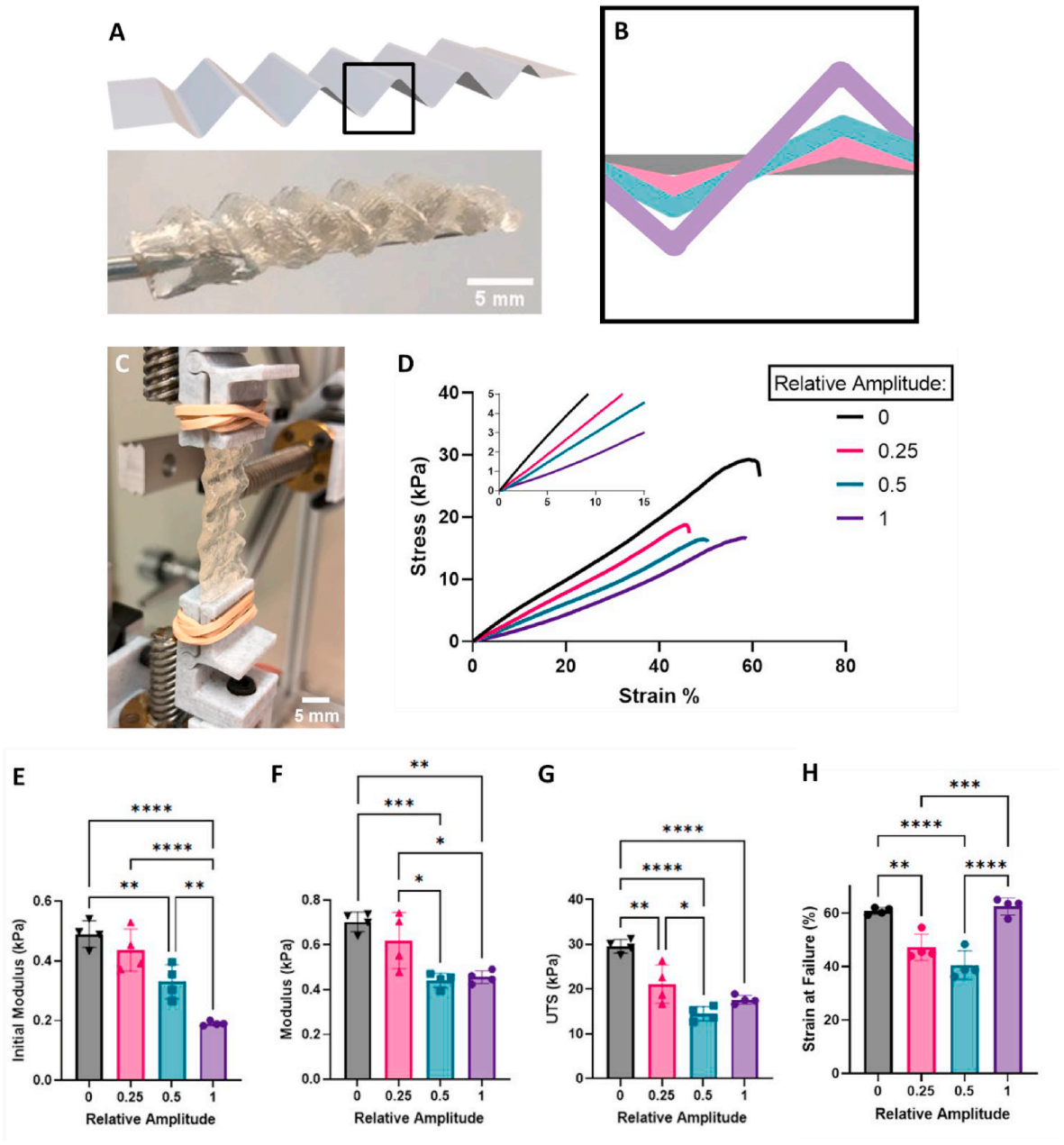

Fig. 4. Impact of non-planar corrugation on print mechanics. (A) 3D model and printed corrugation. (B) Side profile of the four amplitude profiles ranging from flat to 45° angles. (C) Corrugated print mounted on stretch device. (D) Representative stress-strain relationship of when stretched to failure. (E) Modulus at 10% strain. (F) Maximum modulus. (G) Ultimate tensile strength. (H) Strain at failure.

all six paths parallel to the axis of stretch (Fig. 7A–C). Samples in between were printed with alternating layers of different directions. Stretch to failure revealed that when all six layers are aligned with the stretch, the failure strain and stress are higher than any sample with layer(s) perpendicular (Fig. 7D). The more perpendicular paths that are included, the lower the initial modulus, maximum modulus, and ultimate tensile stress (Fig. 7E–G).

3.6. Printing Miura Ori origami structures

The Miura-Ori geometry printed with alginate displays the desired surface features of the original geometry (Fig. 8A and B). When stretched, the unfolding of the structure creates a change in width that is directly related to the depth of the folds (Fig. 8C). The stress response during cyclic stretch decreases with the inclusion of these origami folds, and the deeper the folds are, the lower the stress (Fig. 8D). Additionally, the unloading curve of the flat and 2 mm depth samples reach negative stress near the origin. Measurement of the Poisson's ratio during stretch to 20% strain revealed significant reduction in the ratio of the Miura-Ori prints. 4 mm depth of fold prints have a ratio near zero, meaning that the width of the sample remains constant within this range of stretch (Fig. 8E). 6 mm depth of fold prints have a negative Poisson's ratio.

4. Discussion

Traditional, planar slicers have been required to slice in a plane-by-plane fashion because upper layers require the support of the lower layers to remain in their intended positions. With the advent of embedded printing [16,29], the printed material does not necessarily require that layers below support upper layers because the support bath

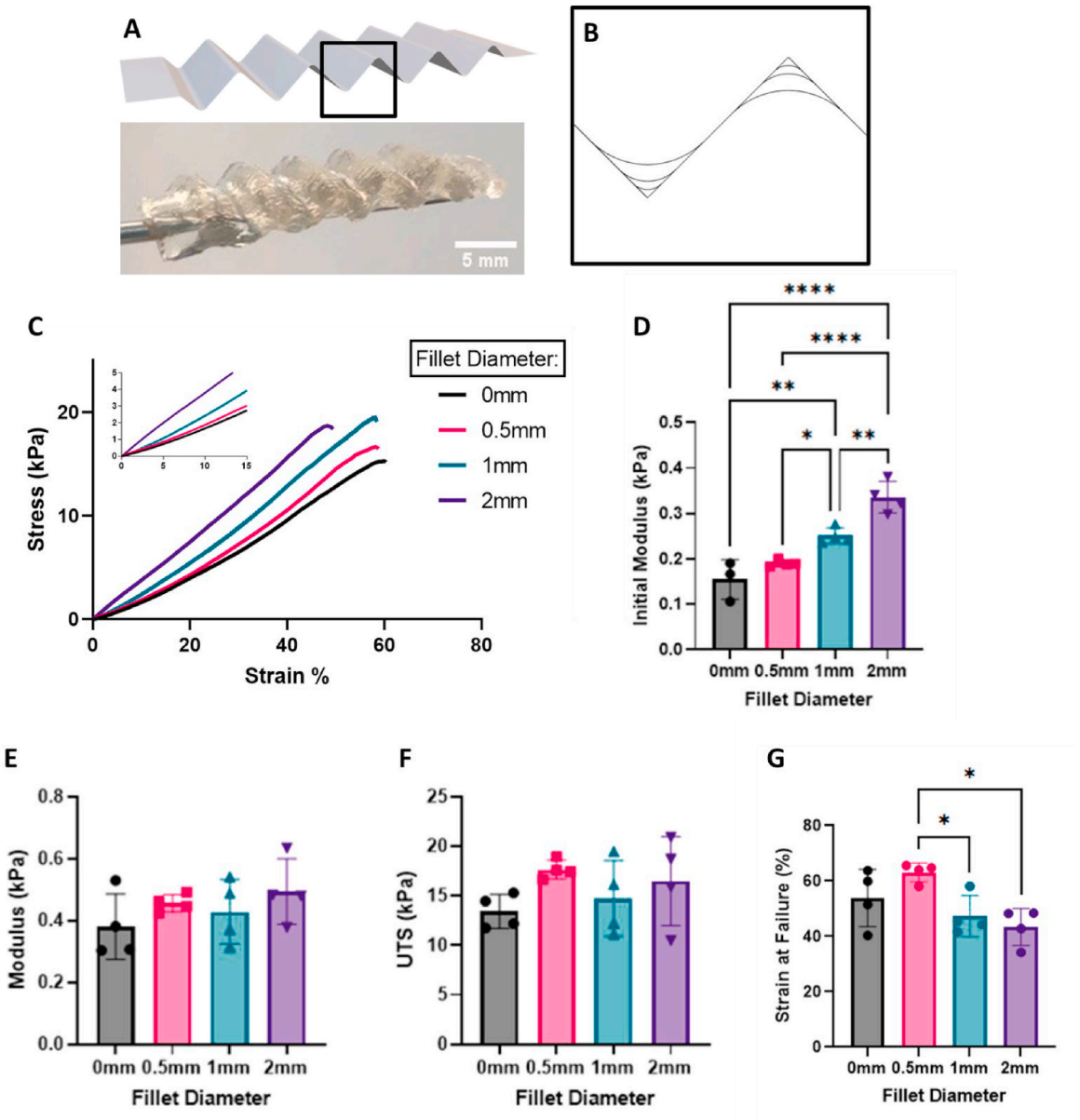

Fig. 5. Impact of corrugation curvature on print mechanics. (A) 3D model and printed corrugation. (B) Side profile of four different fillet diameters found at peaks and valleys of the corrugation. (C) Representative stress-strain relationship of when stretched to failure. (D) Modulus at 10% strain. (E) Maximum modulus. (F) Ultimate tensile strength. (G) Strain at failure.

material maintains the structure, rather than the printed material itself. Novel slicers have been developed to enable highly controlled print path generation [30]; however, no slicer has been developed to take advantage of the flexibility in print direction that embedded printing allows. Our non-planar slicer has been developed with the intention of creating 3D printer-ready files to allow for flexibility in the Z-axis movement of printing, supported by embedded printing methods. The methods demonstrated in this study may be transferrable to creating tunable mechanics for a wide range of bioprinted tissues. In addition, this slicing method creates a means to design thin curved geometries such as heart valve leaflets. Future work will expand into creating heart valves with high fidelity structure and mechanical response.

Because this version of the slicer divides the model into equally spaced sections in the X-Z and Y-Z planes, the effective spacing between parallel paths may not be equal depending on the surface angle. On a sloped surface, the path spacing becomes the hypotenuse of the rise and run, increasing the distance between adjacent paths. Adjusting the path spacing based on angle would be a future feature that may improve consistency of material deposition no matter the surface angle.

4.1. *Effect of extruder direction on alginate extrusion width*

Changes in path width and variability with respect to the printing angle is likely due to the needle passing through or near the bioink as it is extruded, smearing the line. The results demonstrate that print geometries may be limited in their maximum feature angles because of the limitations of downward print angles. Changes in the nozzle shape and size may impact the resulting path by changing the dynamic interaction of the nozzle, ink, and bath material. Designing print models based on limiting the maximum print angle away from horizontal may be key to high fidelity print results. Additionally, designing print paths to be predominantly upward rather than downward may improve print quality by reducing the variation in extrusion width.

Future work in simulating the fluid flow will help us to determine

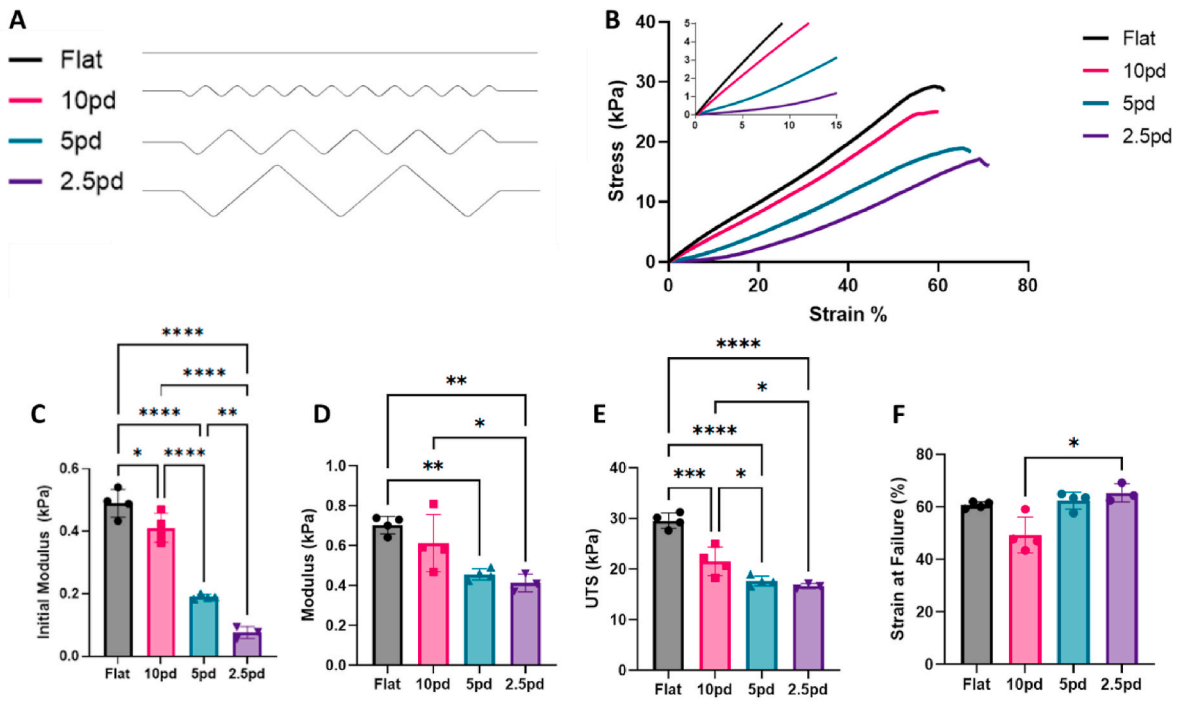

Fig. 6. Size and frequency of corrugation modifies stretch response in low strain regions. (A) Side view of prints designed with varying frequency with angle of corrugation remaining constant (45°). (B) Representative stress-strain relationship of when stretched to failure. (C) Modulus at 10% strain. (D) Maximum modulus. (E) Ultimate tensile strength. (F) Strain at failure.

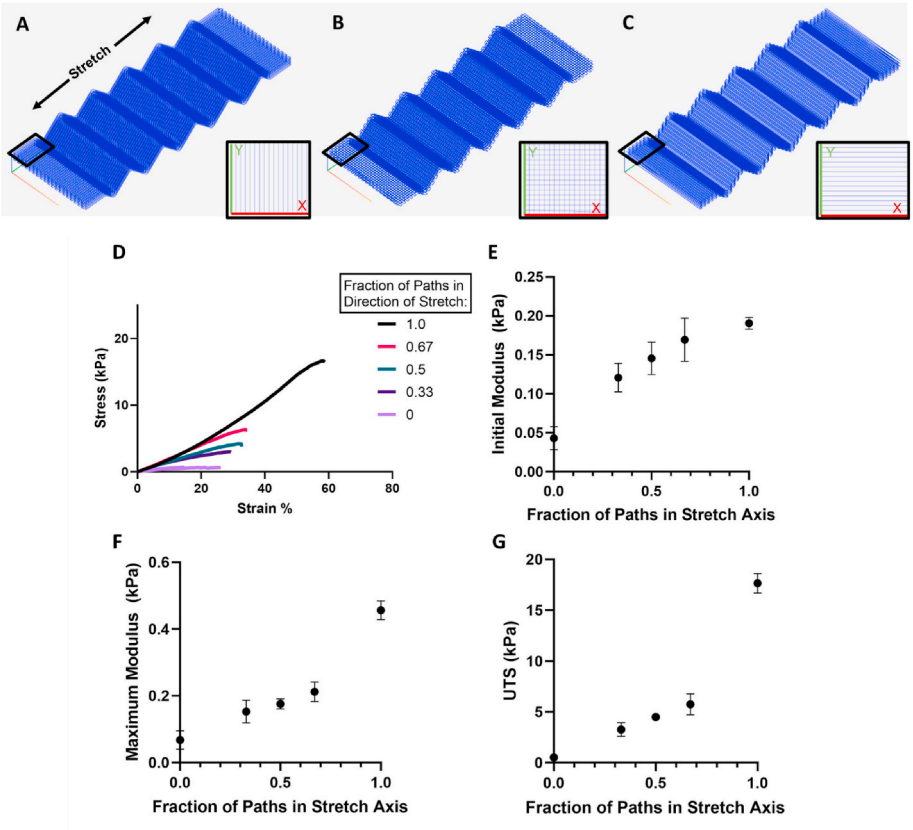

Fig. 7. Varying print path direction across six layers of the print and the effect on stiffness and strength of final print. (A) Prints were designed with the six layer's paths aligned either parallel (B) crosshatching or (C) perpendicular to the direction of stretch. (D) Representative stress-strain relationship of when stretched to failure. (E) Modulus at 10% strain. (F) Maximum modulus. (G) Ultimate tensile strength.

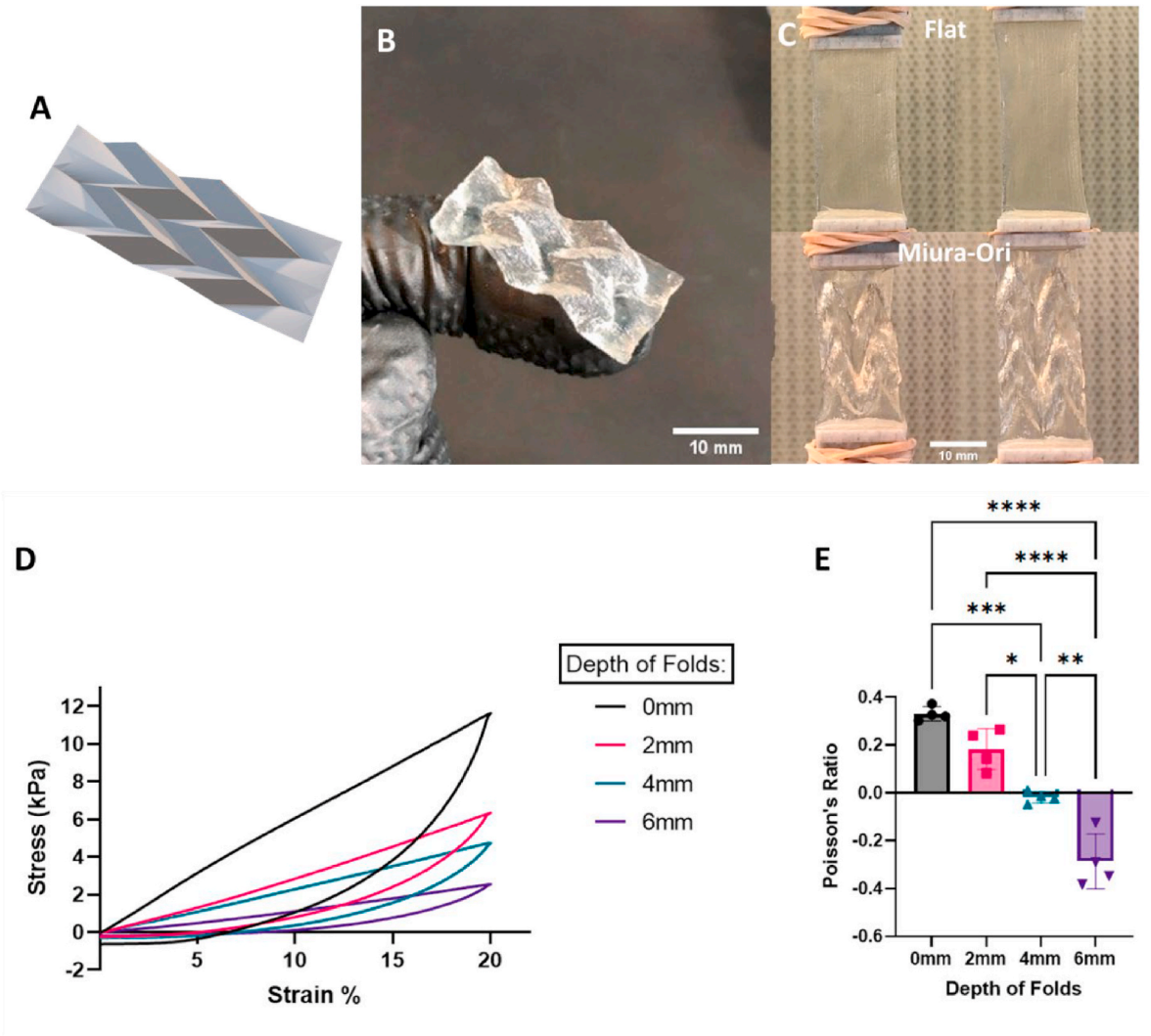

Fig. 8. Non-planar printing of auxetic geometries. (A) Example model of the Miura-Ori folded structure. (B) Printed sample generated from the Miura-Ori model. (C) Flat and Miura-Ori with 6 mm depth of folds unstretched (left) and stretched to 20% strain (right). (D) Representative stretch and release curves of flat and Miura-Ori samples with various depths of folded features. (E) Poisson ratio of flat and Miura-Ori samples.

factors that will help to improve the consistency of print path diameter. Factors such as nozzle shape and size will likely affect the rheology of the extruded material through the bath. Additional studies of the behavior of other printable biomaterials, such as collagen or methacrylated hyaluronic acid, will also develop our understanding of the process based on crosslinking/gelation process and rheology. Bioinks that have previously been demonstrated to behave similarly to 4% alginate solutions with FRESH printing would also likely be able to perform similarly in non-planar printing. Collagen (24 mg/mL), fibrinogen (40 mg/mL), and methacrylated hyaluronic acid (1.5% w/v) are example candidates that have been previously demonstrated with FRESH printing alongside 4% alginate [17].

4.2. Multi-material printing with non-planar and planar slicing

We have demonstrated that, with the non-planar method, we can print multi-material geometries with distinctly different results than traditional slicing methods (Fig. 3). There are several distinct differences between planar and non-planar printing that result in differences in final print results. Because there are two separate materials printed, the printer must switch between extruders to complete each particular layer (Fig. 3E, Video S1). At every material change, the extruder must move completely out of the print bath and be replaced by the other nozzle. Any excess material coming out of these nozzles during the transition may get deposited at the point of entry and exit into the bath.

Supplementary data related to this article can be found at https://doi.org/10.1016/j.bprint.2022.e00242.

Additionally, planar printing necessitates many travel moves during a print of this type of shape. The extruders do not deposit during these moves, but the motion can drag deposited material and any excess oozing can cause stringing between the two points of deposition. This effect can be seen between the peaks of the planar print (Fig. 3E). These disruptions hinder consistent print results and prevent us from being able to compare the mechanical properties of planar prints to those of non-planar prints in the following studies.

In non-planar printing, the layers are very distinct because of a lack of travel moves within a layer, and greatly reduced number of syringe changes. The excessive blending in the valley of the print may be due to material being pushed to low points when the nozzle is moving at a downward angle.

4.3. Mechanics of corrugated alginate prints

Corrugated geometries created out of soft, flexible materials such as hydrogels allow for unfolding of the angular portions up to a certain strain. We created simple corrugations using the non-planar printing

method to understand how we may be able to create geometries that alter the stress-strain relationship to be tunable for towards properties of native tissues [31,32].

Increased amplitude lowers initial modulus due to greater folding length that takes more strain to reach the point of flattening out. Corrugated samples also likely have high stress concentrations at the peaks and valleys of the print that may not be able to fully straighten out before failure, strengthening the idea that the corrugations increase stress concentrations at the peaks and valleys, leading to premature failure compared to flat samples. The trend of strain at failure likely results from flat samples having highly aligned paths with low variance in extruded path width and path spacing. When vertical motion is introduced into the printing, there is more variance in the extrusion as shown in Fig. 2. The increase in failure strain of the samples with a relative amplitude of one is likely due to the overall extendable length of the samples. These 45° corrugations allow spring-like extensions that are able to overcome the loss of strength due to path variation.

Adding a fillet to the corrugation reduces the length of straight sections of hydrogel in the geometry, leading to less of a hinge-like motion at the peaks and valleys and more of a constant, linear, spring-like response to strain. The ultimate tensile stress and strain at failure indicate that the overall stresses are likely similar across these samples, but the added curvature of a small diameter fillet may reduce the stress concentration at the joint by delocalizing the stress. Increasing the fillet further reduces the overall sample length, and even if this reduces the stress concentration further, the loss of overall length seems to be a greater factor in determining strain at failure.

When reducing the periodicity of the corrugations, there are fewer hinge points, and the stress of unfolding is distributed to fewer points, leading to failure at a lower stress. Low initial modulus in low periodicity likely stems from fewer hinge points needing to flex for extension of the sample. If samples were able to perfectly straighten out, the overall modulus would eventually reach levels equal to that of the flat sample; however, the samples fail before reaching that point, indicating that the hinge points remain in the alginate, even at high strain. Corrugated groups do not have a significantly different strain at failure from the flat samples, displaying that these prints can exhibit significantly different stiffness features across the same strain regime as flat samples. The 10 period samples trend towards a decrease in failure strain that may be due to compounding variation in path width because of the high amount of downward print movements.

These studies of corrugated geometries show that strain-stiffening materials can be created out of a homogeneous alginate ink. Including these features can result in tunable stiffness and strain response at both low and high strains. However, balancing the desired stress-strain properties, the failure stress and strain, and the maximum modulus needs to be considered depending on the application needs [33,34].

4.4. Effect of path direction on response to stretch

FRESH bioprinting gradually crosslinks bioinks through aqueous phase of the bath material. In the case of printing alginate, calcium chloride in the print bath diffuses into the bioink to ionically crosslink the alginate [29]. This process is slow enough that adjacent print paths can fuse to one another, but fast enough that paths still contain distinct directionality after washing. We wanted to understand whether this process effects the anisotropy of printed samples.

Aligning print paths along the stretch direction increases stiffness and ultimate stress of the corrugations. These features are likely due to delamination of layers perpendicular to the stress. Stretching perpendicular to the path direction stresses the interfaces between adjacent paths more than the paths themselves resulting in softer materials and earlier yield. This anisotropy depending on path direction may be useful for multi-axial strengthening of tissues such as heart valve leaflets, bladder, and cornea that will be loaded in multiple directions [35,36].

4.5. Printing Miura Ori origami structures

Previous studies have demonstrated applications of auxetic materials in tissue engineering in order to match the aspect ratio changes of tissues under loading [37,38]. Auxetic tissues will become wider in the axis perpendicular to loading during stretch. Previously studied materials have been auxetic because of open gaps in the geometry that allowed for in-plane flexure of the material. The Miura-Ori geometry is a continuous, 3D surface geometry that presents auxetic properties by unfolding, making it optimal for applications where a continuous, solid surface is desired [28].

The reduction of stress in the Miura-Ori prints with respect to fold depth is similar to the trend found from changing the amplitude of corrugated prints. The increased feature size creates greater surface area in the same amount of space, allowing for longer periods of unfolding before the sample flattens out. The negative stress seen during the unloading of the flat and 2 mm depth samples is likely due to alginate crosslinks breaking during stretch and reforming during release [39]. To return to the original resting length, the sample must be compressed. Samples with greater depth of folds do not show this feature, demonstrating that the reduced stress of the folds also reduces sample deformation. The Poisson's ratio of the prints become wider during stretch. These features may be able to reduce off-axis stress if the entire print is constrained and uniaxially stretched. This may be useful for patch-like biomaterial applications, such as cardiac patches, where there is risk of detachment on certain edges of the tissue [40].

5. Conclusions

Manufacturing cell-friendly hydrogels for applications in tissue engineering requires material geometry and mechanical properties to closely match those of the native tissue it replaces. To address this, we developed a method of flexible manufacturing for creating curvature in embedded printing. We have shown that this method can recreate thin, curved geometries with single and dual material printing. We have also shown that the manufacturing process allows for production of non-linear stress-strain relationships within a homogeneous material that may create a more native-like response to stress. Additionally, anisotropic behavior through layer alignment creates a secondary method of property development. These, combined with other complex behaviors, such as negative Poisson's ratio geometry, create an array of techniques in non-planar printing that may improve our ability to replicate native mechanical properties.

Funding sources

This work was supported by funding from the National Science Foundation Graduate Research Fellowship (DGE-1650441), National Institutes of Health R01 HL151190 and R01 HL143247, and by the Cornell Center for Materials Research with funding from the Research Experience for Undergraduates program (DMR-1757420 and DMR-1719875).

CRediT authorship contribution statement

Benjamin J. Albert: Conceptualization, Methodology, Software, Investigation, Writing – original draft. **Coral Wang:** Methodology, Software, Investigation, Writing – review & editing. **Christian Williams:** Methodology, Software, Investigation, Writing – review & editing. **Jonathan T. Butcher:** Conceptualization, Writing – review & editing.

Declaration of competing interest

The authors declare that they have no known competing financial interests or personal relationships that could have appeared to influence

the work reported in this paper.

Data availability

The data is part of an intellectual property disclosure, and will be made available upon completion of prosecution of that disclosure into a Patent.

Appendix A. Supplementary data

Supplementary data to this article can be found online at https://doi.org/10.1016/j.bprint.2022.e00242.

References

[1] H.W. Kang, S.J. Lee, I.K. Ko, C. Kengla, J.J. Yoo, A. Atala, A 3D bioprinting system to produce human-scale tissue constructs with structural integrity, Nat. Biotechnol. 34 (3) (2016) 312–319.

[2] D.B. Kolesky, R.L. Truby, A.S. Gladman, T.A. Busbee, K.A. Homan, J.A. Lewis, 3D bioprinting of vascularized, heterogeneous cell-laden tissue constructs, Adv. Mater. 26 (19) (2014) 3124–3130.

[3] S.V. Murphy, A. Atala, 3D bioprinting of tissues and organs, Nat. Biotechnol. 32 (8) (2014) 773–785.

[4] I.T. Ozbolat, M. Hospodiuk, Current advances and future perspectives in extrusion-based bioprinting, Biomaterials 76 (2016) 321–343.

[5] H. Ravanbakhsh, V. Karamzadeh, G. Bao, L. Mongeau, D. Juncker, Y.S. Zhang, Emerging technologies in multi-material bioprinting, Adv. Mater. 2104730 (2021), 2104730.

[6] J.M. Unagolla, A.C. Jayasuriya, Hydrogel-based 3D Bioprinting: A Comprehensive Review on Cell-Laden Hydrogels, Bioink Formulations, and Future Perspectives, Applied Materials Today, 2019, 100479.

[7] W. Sun, B. Starly, A.C. Daly, J.A. Burdick, J. Groll, G. Skeldon, W. Shu, Y. Sakai, M. Shinohara, M. Nishikawa, J. Jang, D.W. Cho, M. Nie, S. Takeuchi, S. Ostrovidov, A. Khademhosseini, R.D. Kamm, V. Mironov, L. Moroni, I.T. Ozbolat, The bioprinting roadmap, Biofabrication 12 (Issue 2) (2020).

[8] A. Panwar, L.P. Tan, Current status of bioinks for micro-extrusion-based 3D bioprinting, Molecules 21 (6) (2016).

[9] K.S. Lim, J.H. Galarraga, X. Cui, G.C.J. Lindberg, J.A. Burdick, T.B.F. Woodfield, Fundamentals and applications of photo-cross-linking in bioprinting, Chem. Rev. 120 (19) (2020) 10662–10694.

[10] L. Ouyang, Pushing the rheological and mechanical boundaries of extrusion-based 3D bioprinting, Trends Biotechnol. (2022) 1–12.

[11] J.H. Galarraga, M.Y. Kwon, J.A. Burdick, 3D bioprinting via an in situ crosslinking technique towards engineering cartilage tissue, Sci. Rep. 9 (1) (2019) 1–12.

[12] K.S. Lim, B.S. Schon, N.V. Mekhileri, G.C.J. Brown, C.M. Chia, S. Prabakar, G. J. Hooper, T.B.F. Woodfield, New visible-light photoinitiating system for improved print fidelity in gelatin-based bioinks, ACS Biomater. Sci. Eng. 2 (10) (2016) 1752–1762.

[13] L. Ouyang, C.B. Highley, W. Sun, J.A. Burdick, A generalizable strategy for the 3D bioprinting of hydrogels from nonviscous photo-crosslinkable inks, Adv. Mater. 29 (8) (2017).

[14] M. Albanna, K.W. Binder, S.V. Murphy, J. Kim, S.A. Qasem, W. Zhao, J. Tan, I.B. El-Amin, D.D. Dice, J. Marco, J. Green, T. Xu, A. Skardal, J.H. Holmes, J.D. Jackson, A. Atala, J.J. Yoo, In situ bioprinting of autologous skin cells accelerates wound healing of extensive excisional full-thickness wounds, Sci. Rep. 9 (1) (2019) 1–15.

[15] F. Wulle, O. Gorke, S. Schmidt, M. Nistler, G.E.M. Tovar, O. Riedel, A. Verl, A. Weber, A. Southan, Multi-axis 3D printing of gelatin methacryloyl hydrogels on a non-planar surface obtained from magnetic resonance imaging, Addit. Manuf. 50 (December 2021) (2022), 102566.

[16] T. Bhattacharjee, S.M. Zehnder, K.G. Rowe, S. Jain, R.M. Nixon, W.G. Sawyer, T. E. Angelini, Writing in the granular gel medium, Sci. Adv. 1 (8) (2015) 4–10.

[17] A. Lee, A.R. Hudson, D.J. Shiwarski, J.W. Tashman, T.J. Hinton, S. Yerneni, J. M. Bliley, P.G. Campbell, A.W. Feinberg, 3D bioprinting of collagen to rebuild components of the human heart, Science 365 (6452) (2019) 482–487.

[18] L. Ning, R. Mehta, C. Cao, A. Theus, M. Tomov, N. Zhu, E.R. Weeks, H. Bauser-Heaton, V. Serpooshan, Embedded 3D bioprinting of gelatin methacryloyl-based constructs with highly tunable structural fidelity, ACS Appl. Mater. Interfaces 12 (40) (2020) 44563–44577.

[19] M.A. Skylar-Scott, S.G.M. Uzel, L.L. Nam, J.H. Ahrens, R.L. Truby, S. Damaraju, J. A. Lewis, Biomanufacturing of organ-specific tissues with high cellular density and embedded vascular channels, Sci. Adv. 5 (9) (2019).

[20] D.J. Shiwarski, A.R. Hudson, J.W. Tashman, A.W. Feinberg, J.W. Tashman, Emergence of FRESH 3D Printing as a Platform for Advanced Tissue Biofabrication, 010904, APL Bioengineering, 2021. February.

[21] M. Gao, H. Zhang, W. Dong, J. Bai, B. Gao, D. Xia, B. Feng, M. Chen, X. He, M. Yin, Z. Xu, N. Witman, W. Fu, J. Zheng, Tissue-engineered trachea from a 3D-printed scaffold enhances whole-segment tracheal repair, Sci. Rep. 7 (1) (2017) 1–12.

[22] S.E. Gullbrand, D.H. Kim, E. Bonnevie, B.G. Ashinsky, L.J. Smith, D.M. Elliott, R. L. Mauck, H.E. Smith, Towards the scale up of tissue engineered intervertebral discs for clinical application, Acta Biomater. 70 (2018) 154–164.

[23] L.A. Hockaday, K.H. Kang, N.W. Colangelo, P.Y.C. Cheung, B. Duan, E. Malone, J. Wu, L.N. Girardi, L.J. Bonassar, H. Lipson, C.C. Chu, J.T. Butcher, Rapid 3D printing of anatomically accurate and mechanically heterogeneous aortic valve hydrogel scaffolds, Biofabrication 4 (3) (2012).

[24] K.K. Moncal, V. Ozbolat, P. Datta, D.N. Heo, I.T. Ozbolat, Thermally-controlled extrusion-based bioprinting of collagen, J. Mater. Sci. Mater. Med. 30 (5) (2019).

[25] M.E. Prendergast, M. Davidson, J.A. Burdick, A biofabrication method to align cells within bioprinted photocrosslinkable and cell-degradable hydrogel constructs via embedded fibers, Biofabrication (2021) 23, 0.

[26] A.V. Shembekar, Y.J. Yoon, A. Kanyuck, S.K. Gupta, Generating robot trajectories for conformal three-dimensional printing using nonplanar layers, J. Comput. Inf. Sci. Eng. 19 (3) (2019) 1–13.

[27] E. Mirdamadi, J.W. Tashman, D.J. Shiwarski, R.N. Palchesko, A.W. Feinberg, FRESH 3D bioprinting a full-size model of the human heart, ACS Biomater. Sci. Eng. 6 (11) (2020) 6453–6459.

[28] J.L. Silverberg, A.A. Evans, L. McLeod, R.C. Hayward, T. Hull, C.D. Santangelo, I. Cohen, Using origami design principles to fold reprogrammable mechanical metamaterials, Science 345 (6197) (2014) 647–650.

[29] T.J. Hinton, Q. Jallerat, R.N. Palchesko, J.H. Park, M.S. Grodzicki, H.J. Shue, M. H. Ramadan, A.R. Hudson, A.W. Feinberg, Three-dimensional printing of complex biological structures by freeform reversible embedding of suspended hydrogels, Sci. Adv. 1 (9) (2015).

[30] A. Gleadall, FullControl GCode Designer: open-source software for unconstrained design in additive manufacturing, Addit. Manuf. 46 (September 2020) (2021), 102109.

[31] T. Jin, I. Stanciulescu, Numerical investigation of the influence of pattern topology on the mechanical behavior of PEGDA hydrogels, Acta Biomater. 49 (2017) 247–259.

[32] S.M. Mehta, T. Jin, I. Stanciulescu, K.J. Grande-Allen, Engineering biologically extensible hydrogels using photolithographic printing, Acta Biomater. 75 (2018) 52–62.

[33] C.F. Guimarães, L. Gasperini, A.P. Marques, R.L. Reis, The stiffness of living tissues and its implications for tissue engineering, Nat. Rev. Mater. 5 (5) (2020) 351–370.

[34] A. Jafari, Z. Ajji, A. Mousavi, S. Naghieh, S.A. Bencherif, H. Savoji, Latest advances in 3D bioprinting of cardiac tissues, Adv. Mater. Technol. 2101636 (2022), 2101636.

[35] W. Bian, C.P. Jackman, N. Bursac, Controlling the structural and functional anisotropy of engineered cardiac tissues, Biofabrication 6 (2) (2014).

[36] K.D. Dwyer, K.L.K. Coulombe, Cardiac mechanostructure: using mechanics and anisotropy as inspiration for developing epicardial therapies in treating myocardial infarction, Bioact. Mater. 6 (7) (2021) 2198–2220.

[37] Y. Jin, C. Xie, Q. Gao, X. Zhou, G. Li, J. Du, Y. He, Fabrication of multi-scale and tunable auxetic scaffolds for tissue engineering, Mater. Des. 197 (2021), 109277.

[38] P. Mardling, A. Alderson, N. Jordan-Mahy, C.L. Le Maitre, The use of auxetic materials in tissue engineering, Biomater. Sci. 8 (8) (2020) 2074–2083.

[39] J. Li, A.D. Celiz, J. Yang, Q. Yang, I. Wamala, W. Whyte, B.R.R. Seo, N.V. Vasilyev, J.J. Vlassak, Z. Suo, D.J. Mooney, Tough adhesives for diverse wet surfaces, Science 357 (6349) (2017) 378–381.

[40] D. Olvera, M. Sohrabi Molina, G. Hendy, M.G. Monaghan, Electroconductive melt electrowritten patches matching the mechanical anisotropy of human myocardium, Adv. Funct. Mater. 30 (44) (2020).